CrossMark

Inferring grain boundary structure–property relations from effective property measurements

Oliver K. Johnson[1] · Lin Li[2] · Michael J. Demkowicz[1] · Christopher A. Schuh[1]

Abstract Grain boundaries strongly affect many materials properties in polycrystalline materials. However, very few structure–property models exist for grain boundaries, due in large part to the complicated and poorly understood way in which the properties of grain boundaries vary with their crystallographic structure. In the present work, we infer grain boundary structure–property correlations from measurements of the effective properties of a polycrystal. We refer to this approach as grain boundary properties localization. We apply this technique to a simple model system of grain boundary diffusivity in a two-dimensional microstructure, and infer the properties of low- and high-angle grain boundaries from the effective diffusivity of the grain boundary network. The generalization and use of these methods could greatly reduce the computational and experimental effort required to establish structure–property correlations for grain boundaries. More broadly, the technique of properties localization could be used to infer the properties of many microstructural constituents in complex microstructures.

✉ Oliver K. Johnson
  ojohnson@mit.edu

  Lin Li
  lin.li@eng.ua.edu

  Michael J. Demkowicz
  mikejd@mit.edu

  Christopher A. Schuh
  schuh@mit.edu

[1] Department of Materials Science and Engineering, Massachusetts Institute of Technology, 77 Massachusetts Ave, Cambridge, MA 02139, USA

[2] Department of Materials and Metallurgical Engineering, University of Alabama, Tuscaloosa, AL 35487, USA

Introduction

The effective properties of polycrystalline materials are influenced, and in some cases dominated, by the character and connectivity of grain boundaries. For example hydrogen embrittlement [1], corrosion [2], creep [3], weldability [4], and superconductivity [5] all depend strongly on the structure and spatial arrangement of grain boundaries in the microstructure. Great effort has been invested by the scientific community to correlate grain boundary structure and properties, but simple constitutive relations have been elusive.

One fundamental difficulty stems from the complex structure of grain boundaries, whose description requires, at a minimum, the specification of five crystallographic parameters [6]. Three of these define the lattice misorientation between adjacent grains and the other two specify the interfacial plane. In addition, there are microscopic degrees of freedom related to in-plane translations and associated structural relaxations [7–9], though these will be neglected in the present study.

Another obstacle to correlating grain boundary structure with materials properties is the difficulty of controlled grain boundary synthesis. Controlled production of grain boundaries in metals has predominantly been performed via seeded growth of bicrystals from the melt [10–12]. Single-crystal seeds are first synthesized, then cut and oriented appropriately, after which bicrystals can be grown from the melt by, e.g., the vertical Bridgman method [10, 11]. Other techniques include sintering of metalic thin films [13, 14], and the direct bonding technique for thin films of brittle materials [15–17]. In these techniques, single crystals are first produced and aligned relative to one another, and then bonded either by hot pressing, in the case of metals, or through evaporation of an intermediate water

layer (after a number of meticulous surface preparation steps). Regardless of the method, controlled preparation of even a single grain boundary involves numerous steps, sophisticated equipment, and a significant time investment.

Though still requiring significant time, atomistic simulations can be employed to ameliorate some of the experimental difficulties and sources of error, as well as increase throughput [18–20]. However, such simulations are not without their own complications. Accurate interatomic potentials are not available for all materials and the development and validation of new models is a significant undertaking. Moreover, the computational cost of atomistic simulations restricts one to the investigation of small material volumes. This places a fundamental limitation on the number and types of grain boundaries that can be considered.

The largest catalog of grain boundary property data to date consists of calculated excess energies and mobilities for 388 grain boundaries in four different metals [18–20]. While this constitutes a significant milestone, a sample of $\mathcal{O}(10^2)$ points in a five-dimensional space is still relatively sparse coverage. A brute force attempt to explore the space adequately, whether by experimental or computational means, remains impractical due to the resources that would be required.

In contrast to the difficulties of synthesizing and studying individual grain boundaries, it is relatively easy to produce polycrystalline samples. Commercial solutions now permit crystallographic characterization of sample areas large enough to capture millions of grain boundaries. Automated electron backscatter diffraction (EBSD) techniques allow for the rapid characterization of four of the five grain boundary parameters for every boundary that terminates at the sample surface. For microstructures with through-thickness grains, and where out of plane curvature can be neglected, the final parameter can be obtained by correlating EBSD scans on opposite faces of the sample [21], or by comparing intensities of overlapping Kikuchi patterns with interaction volume models [22]. For general microstructures, serial sectioning methods or high energy diffraction techniques [23] may be used.

The relative ease of synthesizing and characterizing polycrystals suggests an alternative route to obtain grain boundary structure–property correlations, beyond the one-by-one study of individual bicrystals. For a grain boundary-sensitive property in a polycrystal, the global effective response of the grain boundary network is the result of a homogenization of the local properties of the constituent grain boundaries. This is analogous to an electrical resistor network where the effective resistance of the circuit depends upon the component resistances and the topology of the network. If one measures the effective resistance of such an electrical network, then, under certain circumstances, it may be possible to deduce the resistance values of the components. If one can, similarly, infer the local properties of grain boundaries in a polycrystalline aggregate from measurements of the macroscopic effective response of the network, it would facilitate a more efficient approach to searching the five-dimensional grain boundary structure space for structure–property correlations.

The process of deconvoluting local quantities of a heterogeneous system from homogenized global measurements is broadly referred to as *localization*. While this concept is not new, the use of localization techniques in materials science has, until now, been limited to the calculation of local field quantities, e.g., stress, in the presence of an applied macroscopic field [24–31], or single-crystal elastic constants [32–34]. In this paper, we address a new kind of localization problem, in which the goal is to determine the local materials properties of grain boundaries from measured effective (macroscopic) properties of a polycrystal. We also establish a general unifying framework for materials properties localization in the context of any materials property and any relevant microstructural feature. For the case of grain boundary properties localization, we consider a highly simplified two-dimensional polycrystalline model system and attempt to infer the diffusivity of low- and high-angle grain boundaries from the effective diffusivity of the grain boundary network. While this model problem does not represent a general microstructure, its simplicity permits us to identify the important qualitative features that we would expect to observe in other microstructures.

Model

Our model microstructure was similar to that of Chen [35], consisting of a two-dimensional honeycomb lattice (as shown schematically in Fig. 1) containing 6889 hexagonal grains and 20,212 grain boundaries. Crystal orientations were sampled from two-dimensional orientation distribution functions (ODFs) of the following form (see also Fig. 2):

$$f(\theta) = \begin{cases} (2\theta_{max})^{-1} & \text{for} \quad \theta \in [-\theta_{max}, \theta_{max}] \\ 0 & \text{otherwise} \end{cases} \quad (1)$$

and assigned in a spatially uncorrelated manner. In Eq. 1, $\theta_{max} \in [0, \pi/s]$ is a parameter that defines the sharpness of the texture, and s represents the order of the appropriate symmetry point group. In the present study, we considered triclinic crystals having a common $\langle 001 \rangle$ rotation axis parallel to the sample normal direction, for which $s = 1$.
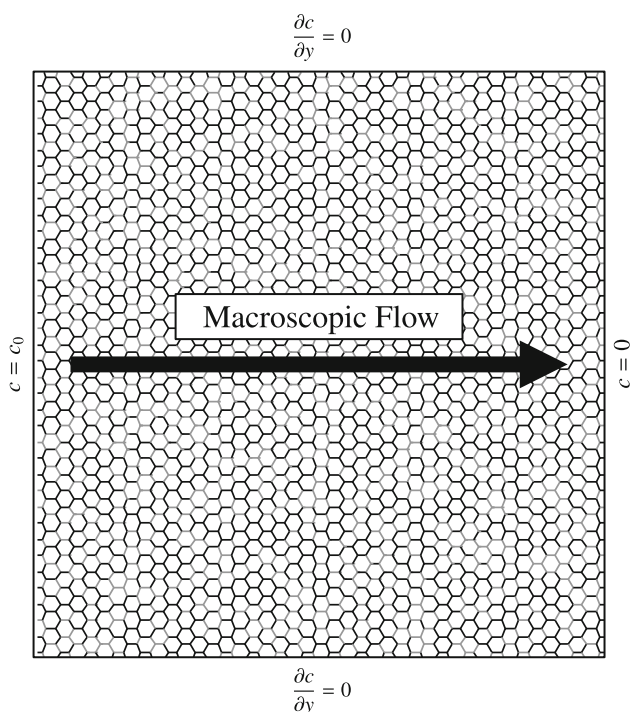
Fig. 1 Schematic plot of the model microstructure showing the boundary conditions used for the diffusion simulations
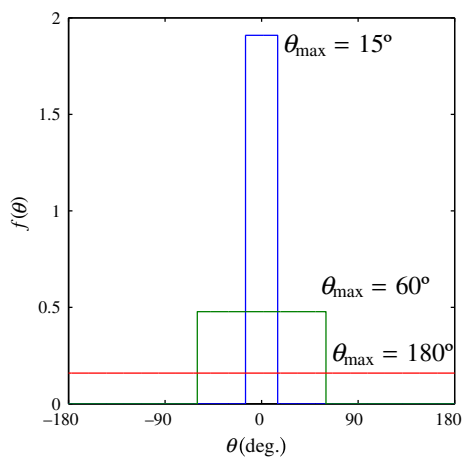
Fig. 2 Two-dimensional ODFs with varying θ_{max} according to Eq. 1

Grain boundary diffusivities were assigned according to the disorientation angle, ω, between neighboring grains with

$$D(\omega) = \begin{cases} D_1 & \text{for } \omega \leq \omega_t \\ D_2 & \text{for } \omega > \omega_t \end{cases}, \qquad (2)$$

where ω is the disorientation angle, ω_t is the threshold angle between low- and high-angle grain boundaries, and $D_1 \leq D_2$ are the low- and high-angle diffusivities, respectively. While the physical properties of grain boundaries are known to depend, in some cases strongly, on the grain

boundary plane inclination [36], our model constitutive equation neglects this dependence. This simplifying assumption, together with the binary classification of grain boundaries into low- and high-angle classes, facilitate tractability and clarity of exposition and can be improved upon in future work.

The boundary conditions, assumptions, and procedure for calculating the effective diffusivity of the grain boundary network were the same as those used by Chen [35]. For our simulations, we assumed that diffusion occured only along the grain boundaries. This simplification is a good approximation in situations for which the microstructure, experimental conditions, and kinetic regime are such that grain boundary diffusion is the dominant pathway and all others (e.g., bulk, surface, dislocation, etc.) can safely be ignored. Alternatively, as mentioned by Chen, these results can be interpreted as simply providing the contribution of grain boundary diffusion to the overall diffusion [35]. The concentration of the diffusing species was fixed at $c = c_0$ and $c = 0$ at the left and right sides of the network, respectively, and zero-flux conditions were imposed at the top and bottom (Fig. 1). Steady-state diffusion was considered, and conservation conditions were enforced at triple junctions (i.e., no material accumulation at triple junctions was permitted). This resulted in a linear system of equations that was solved to obtain the concentrations at each triple junction and, thus, the concentration gradient and local flux along each grain boundary. By averaging the microscopic grain boundary fluxes over any vertical section of the network, we obtained the effective macroscopic diffusion flux, J_{eff}, of the network [35]. Finally, the effective diffusivity, D_{eff}, was calculated by dividing J_{eff} by the macroscopic concentration gradient of the network [35]. By varying the sharpness of the textures (θ_{max}), we obtained grain boundary networks with different grain boundary character distributions, described by the fraction of high-diffusivity grain boundaries, p_2, and, consequently, different values of D_{eff}. We performed simulations using 51 different textures with θ_{max} varying between 7.5° and 180° (see Fig. 2). The reported values of D_{eff} are the median of 1000 network realizations for each texture. Figure 3 shows the effective diffusivity, D_{eff}^{SIM} that was obtained via simulation, as a function of the fraction of high-diffusivity boundaries, p_2, with $D_1 = 10^0$ m²/s, $D_2 = 10^7$ m²/s, and $\omega_t = 15°$.

Based on the values we obtained for D_{eff}, and a knowledge of the crystallographic details of the microstructure—including the crystal orientations, and the resulting grain boundary misorientations—we would like to infer the parameters of our constitutive equation (D_1, D_2, and ω_t). This inverse problem of grain boundary properties localization is tantamount to determining the local

diffusivity of each type of boundary from measured values of the effective network diffusivity.

Strategy

Overview

The relationship between the properties of a material and its microstructure can be expressed as a functional of the following form:

$$\bar{P} = H(M, P), \tag{3}$$

where $\bar{P}$ is the macroscopic effective property of interest, M contains microstructural information, P is a representation of the relevant local constitutive equation, and H is a homogenization relation. Equation 3 can be used in several ways:

Materials properties prediction

In materials properties prediction the microstructure (M) is known, as is the constitutive equation (P), and one evaluates Eq. 3 to obtain the unknown effective property ($\bar{P}$). A common example of this is the prediction of the effective elastic constants of a polycrystal.

Materials design

In materials design, a target effective property ($\bar{P}$) is specified, the constitutive equation (P) is assumed to be known, and Eq. 3 is solved for the unknown microstructure (M) that is commensurate with the target effective property.

Materials properties localization

Materials properties localization completes this set of materials problems by asking the following question: "Having characterized a heterogeneous microstructure (M), and measured its effective properties ($\bar{P}$), is it possible to infer the unknown local properties of its constituents (P)?"

These applications and the known and unknown variables in each case are summarized in Table 1.

In the context of the present model problem, $\bar{P} = D_{\text{eff}}$. For real microstructures, it could be obtained experimentally using, e.g., accumulation methods [37, 38]. From Eq. 2, the parameters of the proposed constitutive relation are $P = [D_1, D_2, \omega_t]^{\mathrm{T}}$. As will be explained subsequently, the relevant microstructural parameters for the grain boundary diffusion problem are $M = [J_1, J_2, J_3]^{\mathrm{T}}$, where $\{J_i \mid i \in [0, 3]\}$ are called triple junction fractions and denote the population of triple junctions coordinated by i "special" grain boundaries [39–47], which, for our purposes,

Table 1 Summary of the applications of Eq. 3

Application	$\bar{P}$	M	P
Prediction	?	✔	✔
Design	✔	?	✔
Localization	✔	✔	?

In this table $\bar{P}$ is the macroscopic effective property of interest, M is the microstructure, and P represents the relevant local constitutive equation (i.e., the local properties). The '?' symbol indicates the unknown quantity that is to be solved for in a given application, and the '✔' symbol indicates a known or specified quantity

correspond to low-angle grain boundaries with diffusivity D_1. The elements of M are easily measured experimentally using various destructive [48–50] or non-destructive [23, 51–54] crystallographic characterization techniques. Because $\sum_i J_i = 1$, only three of the four J_i appear in M.

Homogenization

The specific form of $H(M, P)$ is of critical importance for accurate predictions of $\bar{P}$ in the forward problem of homogenization, and consequently is also crucial for solving the inverse problem of localization. One common form of $H(M, P)$ is the standard effective medium theory (EMT) [35, 55]. EMT works well in systems for which the variation in the local material property values (property contrast) is small [35, 56]. However, in situations where the local values of a material property differ significantly from point to point, the detailed structure of the medium dominates the effective response [35, 56]. In such cases, the true effective property values exhibit a sharp transition at the percolation threshold that EMT models fail to capture.

Experimental measurements of grain boundary diffusivity in bicrystals as a function of disorientation angle have demonstrated that the difference between the minimum and maximum diffusivities can span many orders of magnitude [57]. Because of this strong contrast in the spectrum of grain boundary diffusivities, standard EMT predictions for D_{eff} are inadequate [56]. Reference [35] demonstrated that the phenomenological Generalized Effective Medium (GEM) equation, proposed by [58, 59], provides quantitatively accurate predictions of D_{eff} across a broad range of contrast ratios (from 5 to 10^8) when compared to simulation results [35]. The GEM is an implicit relation that combines aspects of effective medium theory and percolation theory, and may be expressed as[1]

---

[1] There are two distinct concepts of effective diffusivity (or conductivity) in the literature. One is the diffusivity of the actual heterogeneous network as a whole, and the other is the diffusivity of a single boundary in a hypothetical homogeneous sample whose network diffusivity matches that of the real sample. The two notions

$$p_1 \frac{D_1^{1/s} - (2D_{\text{eff}})^{1/s}}{D_1^{1/s} + \left(p_{c,2}^{-1} - 1\right)(2D_{\text{eff}})^{1/s}}$$
$$+ p_2 \frac{D_2^{1/t} - (2D_{\text{eff}})^{1/t}}{D_2^{1/t} + \left(p_{c,2}^{-1} - 1\right)(2D_{\text{eff}})^{1/t}} = 0 \qquad (4)$$

where p_i is the fraction of grain boundaries exhibiting diffusivity D_i, and $p_{c,i}$ is the percolation threshold for the ith grain boundary type. The values of the critical exponents s and t are generally considered to be universal, depending only on the dimensionality of the problem. For the present case, we use $s = 1.09$ and $t = 1.13$. These values differ slightly from those given in [35], however, we found that small deviations in the numerical values of s and t did not affect the results of the GEM significantly and the value of $p_{c,2}$ proved to be of much greater moment. Equation 4 can be solved numerically, using, e.g., bisection methods [35] to obtain D_{eff} as a function of D_1, D_2, and the microstructural parameters p_i and $p_{c,2}$.

To validate the GEM for use as our homogenization relation, we computed D_{eff} using Eq. 4 for each of the simulated textures. We denote the effective diffusivity predicted by Eq. 4 as $D_{\text{eff}}^{\text{GEM}}$, to distinguish it from the values that were obtained directly from our simulations, $D_{\text{eff}}^{\text{SIM}}$. The agreement between the predicted and simulated diffusivities is excellent (see Figs. 3, 4). Strictly speaking, Eq. 4 holds only for infinite systems, and a scaling factor should be used for finite microstructures. However, the value of the scaling factor for our simulations is very close to unity (see [35]), particularly after considering 1000 replications of each microstructure, and we therefore omit it.

Microstructural parameters

An important quantity that appears in the GEM is the percolation threshold, $p_{c,2}$. For a randomly assembled two-dimensional honeycomb network, the percolation threshold is known analytically to be $p_c = 1 - \sin(\pi/18) \approx 0.6527$ [60]. However, the spatial distribution of grain boundary types in real polycrystals is markedly non-random as a result of crystallographic constraints [61]. The resulting local correlations lead to a shift in the percolation threshold [61] and, consequently, must be accounted for in order to obtain accurate predictions of D_{eff}. These short-range correlations can be quantified using the triple junction fractions, J_i. Frary and Schuh obtained an empirical relation that predicts the percolation threshold for two-dimensional networks from the J_i [62]. As mentioned earlier, we are interested in the percolation threshold for type-2
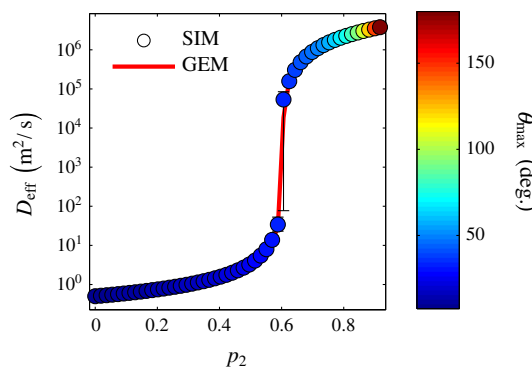
Fig. 3 Effective diffusivity of simulated grain boundary networks for various fractions of type-2 (high-diffusivity) grain boundaries. The *error bars* for many of the microstructures are smaller than the markers, and, as expected, they are very large near the percolation threshold. *Marker color* corresponds to the sharpness of the texture. As θ_{max} was varied, we obtained networks with $D_{\text{eff}}^{\text{SIM}}$ ranging from $\sim 5 \times 10^{-1}$ m²/s to $\sim 5 \times 10^6$ m²/s. The *red solid line* connects the values predicted using $D_{\text{eff}}^{\text{GEM}}$. This is shown as a *solid line* rather than discrete markers only to improve visibility (Color figure online)
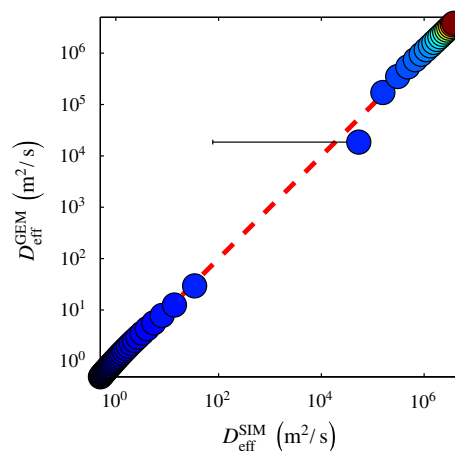
Fig. 4 Comparison of the effective diffusivity predicted by the GEM, $D_{\text{eff}}^{\text{GEM}}$, to that obtained via simulation, $D_{\text{eff}}^{\text{SIM}}$. The *dashed red line* indicates a 1:1 relationship (i.e., perfect agreement). Error bars for many of the data points are smaller than the respective markers. *Marker color* indicates the sharpness of the texture, and is referenced to the color scale of Fig. 3 (Color figure online)

grain boundaries, $p_{c,2}$, but the common convention defines the J_i as the fraction of triple junctions coordinated by i type-1 (low-angle) grain boundaries. In this case, the percolation threshold can be approximated by a second order polynomial of two variables[2]:

$$p_{c,2} = d_1 + d_2\chi + d_3\chi^2 + d_4\sigma + d_5\chi\sigma + d_6\sigma^2 \qquad (5a)$$

with the values of the coefficients, d_j given in Table 2. The

---

Footnote 1 continued

are related and we take the former interpretation, which is the reason that Eq. 4 differs from the form appearing in [35, 58, 59].

---

[2] There is an error in this formula as printed in [62]. If the values of the d_j presented in Table II of [62] are to be used, then the signs of all terms in Eq. 8 of [62] should be positive. This is corrected in Eq. 5a of the present work.

Table 2 Numerical values of the coefficients appearing in Eq. 5a

j	1	2	3	4	5	6
d_j	0.6527	0.0651	0.0117	−0.0961	0.0233	−0.0715

variables σ and χ are topological order parameters, the prior measuring the tendency of grain boundaries of differing types to segregate or form ordered arrangements, and the latter indicating the tendency for grain boundaries of like type to be found in elongated or compact clusters. These are defined in terms of certain ratios of the J_i according to

$$\sigma = \begin{cases} 1 - j_\sigma & \text{for } j_\sigma \leq 1 \\ j_\sigma^{-1} - 1 & \text{for } j_\sigma > 1 \end{cases} \tag{5b}$$

$$\chi = \begin{cases} 1 - j_\chi & \text{for } j_\chi \leq 1 \\ j_\chi^{-1} - 1 & \text{for } j_\chi > 1 \end{cases} \tag{5c}$$

$$j_\sigma = \left(\frac{J_1 + J_2}{J_0 + J_3}\right)\left(\frac{J_{0r} + J_{3r}}{J_{1r} + J_{2r}}\right) \tag{5d}$$

$$j_\chi = \frac{J_1}{J_2}\frac{J_{2r}}{J_{1r}}, \tag{5e}$$

where Eq. 5e is the reciprocal of the expression given in [62] because we are considering $p_{c,2}$. In Eqs. 5d and 5e, the J_{ir} are the triple junction fractions for a randomly assembled network (i.e., in the absence of crystallographic constraints), and are given by a binomial distribution:

$$J_{ir} = \binom{3}{i}(1 - p_1)^{3-i}p_1^i \tag{6}$$

Consideration of Eq. 5 reveals that if a grain boundary network was to be totally uncorrelated then $J_i = J_{ir}$ and $\sigma = \chi = 0$ resulting in $p_{c,2} = d_1$, which is the percolation threshold for the random network. Correlations in the grain boundary network result from the physical requirements of crystallographic constraints as well as other influences such as, e.g., crystallographic texture. Our simulations are crystallographically consistent and, therefore, include both of these effects. The strength and type of these correlations are reflected in the non-random values of the J_i, which, in turn, lead to non-zero values of the order parameters σ and χ and a commensurate shift in the percolation threshold due to the additional terms in Eq. 5a.

The other microstructural parameters in the GEM (Eq. 4) are the p_i. These may also be expressed in terms of the J_i according to [47]

$$p_1 \approx \frac{1}{3}J_1 + \frac{2}{3}J_2 + J_3 \tag{7}$$

and

$$p_1 + p_2 = 1, \tag{8}$$

where the approximation becomes exact in the limit of infinite systems (or for finite systems with periodic boundary conditions). Thus, for the present model system, the relevant details of the microstructure are fully specified by the J_i and we have $\boldsymbol{M} = [J_1, J_2, J_3]^{\mathrm{T}}$.

It is important to note, however, that the J_i also have a subtle dependence on the parameters of the constitutive equation. As mentioned earlier, the J_i are defined as the fraction of triple junctions coordinated by i low-angle grain boundaries (type-1 in the present model); however, the distinction between type-1 and type-2 boundaries is governed by the constitutive parameter ω_t. As a result, not only do the J_i depend upon the value of ω_t, but so do the p_i, and $p_{c,2}$. This interaction between the constitutive parameters, $\boldsymbol{P}$, and the microstructural parameters, $\boldsymbol{M}$, complicates the solution of this particular localization problem. For each trial value of ω_t the microstructure must be re-analyzed: the J_i must be determined anew, and the p_i and $p_{c,2}$ must be recomputed before $H(\boldsymbol{M}, \boldsymbol{P})$ can be evaluated. This does not preclude solution of the localization problem, but care must be taken not to exclude this feedback loop from the solution process.

Localization

The solution of the localization problem is accomplished by solving Eq. 3 for the unknown constitutive parameters of $\boldsymbol{P}$. However, if one considers $\bar{\boldsymbol{P}}$ and $\boldsymbol{M}$ of only a single microstructure then the system will be underdetermined if $\boldsymbol{P}$ contains more than one parameter, as in the present case. Even if the number of microstructures, N, is equal to the number of parameters, n_p, errors arising from imperfect measurements or inexact homogenization models (H) could still preclude the solution of the resulting system of equations. A more flexible approach is to minimize the total error, in some sense, between the measured values of $\bar{\boldsymbol{P}}$ and the predicted values of $H(\boldsymbol{M}, \boldsymbol{P})$ for a large number, N, of microstructures, over the domain of $\boldsymbol{P}$. For the present problem this can be stated as

$$\begin{aligned} \underset{\boldsymbol{P}}{\text{minimize}} \quad & E(\boldsymbol{P}) \\ \text{subject to} \quad & 0 \leq D_1, D_2 \quad , \\ & 0 \leq \omega_t \leq \pi/s \end{aligned} \tag{9}$$

where $E(\boldsymbol{P})$ is a function that provides some measure of the total error. One choice of objective function is the sum of squared errors over all N measurements; however, given that the values of D_{eff} vary over many orders of magnitude, such a procedure would give too much weight to errors at the high end of the D_{eff} spectrum. For instance, a difference of 10^{-3} m²/s is small when $D_{\text{eff}} = \mathcal{O}(10^0)$ m²/s, and a difference of 10^3 m²/s is small when $D_{\text{eff}} = \mathcal{O}(10^6)$ m²/s, but the magnitude of the error in the latter case would completely dominate so that measurements for small D_{eff}

would have negligible influence on the solution. To correct for this effect, we defined the following objective function:

$$
\begin{aligned}
E(\boldsymbol{P}) &= \frac{1}{N}\sum_{i=1}^{N}\left[\log\left(^{(i)}D_{\text{eff}}^{\text{SIM}}\right) - \log\left(^{(i)}D_{\text{eff}}^{\text{GEM}}(\boldsymbol{P})\right)\right]^2 \\
&= \frac{1}{N}\sum_{i=1}^{N}\left[\log\left(\frac{^{(i)}D_{\text{eff}}^{\text{SIM}}}{^{(i)}D_{\text{eff}}^{\text{GEM}}(\boldsymbol{P})}\right)\right]^2
\end{aligned}
\tag{10}
$$

where $^{(i)}D_{\text{eff}}^{\text{SIM}}$ and $^{(i)}D_{\text{eff}}^{\text{GEM}}$ are the effective diffusivities of the ith microstructure (i.e., one of the 51 possible textures) as calculated via simulation and as predicted from the GEM homogenization relation, respectively. Equation 10 represents a least-squares type measure of the error between the logarithms of the effective diffusivities obtained via simulation and those predicted by the GEM for a fixed set of parameter values, $\boldsymbol{P}$, when considering N different microstructures. Using Eq. 10 as the objective function, we solved Eq. 9 in order to infer $\boldsymbol{P}$ from the observed values of $^{(i)}D_{\text{eff}}^{\text{SIM}}$. Physically, this corresponds to a situation in which we have characterized the J_i of N different microstructures, and measured the effective diffusivity of their respective grain boundary networks ($^{(i)}D_{\text{eff}}^{\text{SIM}}$ for $i \in [1, N]$). We then want to know what values of $\boldsymbol{P} = [D_1, D_2, \omega_t]^{\text{T}}$ are commensurate with our observations. In this way, we can infer the local grain boundary properties (D_1 and D_2) from measurements of the macroscopic effective properties ($^{(i)}D_{\text{eff}}^{\text{SIM}}$).

In an effort to visualize the solution space, and to avoid uncertainty resulting from questions of convergence, we employed a brute force method by evaluating Eq. 10 over a grid of points, $\Lambda = \mathcal{D}_1 \times \mathcal{D}_2 \times \Omega_t$, with $\mathcal{D}_1 = \{10^{-8}, 10^{-7.5}, \ldots, 10^8\}$ m²/s, $\mathcal{D}_2 = \{10^{-8}, 10^{-7.5}, \ldots, 10^{12}\}$ m²/s, and $\Omega_t = \{0°, 1.5°, \ldots, 45°\}$. The resolution of this grid defines the precision of our solutions. For each $N \in \{3, 5, 10, 20, 50\}$, we selected N textures uniformly at random from those that were simulated and evaluated Eq. 10 over Λ. This procedure was performed 100 times for each N. Figure 5 depicts isosurfaces through the solution space for constant values of $E(\boldsymbol{P})$, with $N = 3$, and illustrates that $E(\boldsymbol{P})$ decreases monotonically to its global minimum near the true values of $D_1 = 10^0$ m²/s, $D_2 = 10^7$ m²/s, and $\omega_t = 15°$.

Discussion

In the context of a general localization problem in which the true parameter values of a proposed constitutive relation are not known *a priori*, one seeks to infer them while
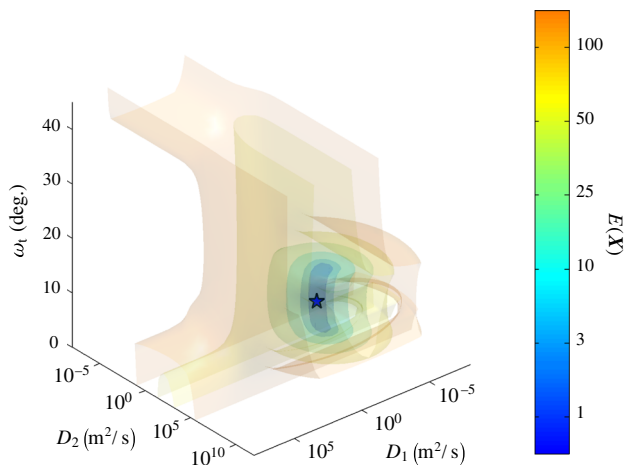
Fig. 5 Isosurfaces through the solution space of $E(\boldsymbol{P})$, with $N = 3$ and $\boldsymbol{P} \in \Lambda$, where $\Lambda = \mathcal{D}_1 \times \mathcal{D}_2 \times \Omega_t$ is a grid of points defined by $\mathcal{D}_1 = \{10^{-8}, 10^{-7.5}, \ldots, 10^8\}$ m²/s, $\mathcal{D}_2 = \{10^{-8}, 10^{-7.5}, \ldots, 10^{12}\}$ m²/s, and $\Omega_t = \{0°, 1.5°, \ldots, 45°\}$. The true values of the parameters are represented by the location of the *blue star* (Color figure online)

simultaneously minimizing experimental/computational expense and effort. In order to accomplish this, one would naturally ask (1) "What is the minimum number of polycrystalline microstructures that I need to consider?" and (2) "What characteristics should those microstructures possess to facilitate the solution of the localization problem?." General answers to these questions are not yet known for arbitrary microstructures and properties and they are subjects worthy of future inquiry. However, some insight into these issues can be gained by considering the simplified and specific case at hand.

With respect to the number of microstructures required, the theoretical minimum, $N_{\min}$, is equal to n_p, the number of parameters in $\boldsymbol{P}$, if the form of the constitutive equation is known. However, multiple copies of an identical microstructure would be redundant and would not permit the solution of the localization problem. Distinct microstructures whose structures are statistically equivalent would also exhibit this redundancy. Consequently, there must be at least as many non-redundant microstructures— i.e., microstructures that are, in some sense, different enough—as there are parameters in $\boldsymbol{P}$. We did not explicitly investigate the influence of the size of the microstructures used for localization. However, we note that in addition to having a sufficient number of non-redundant microstructures, each one should be large enough to satisfy any assumptions (e.g., statistical homogeneity) implicit in the chosen homogenization relation. As illustrated in Fig. 5, it was, indeed, possible to recover the true parameter values to within the resolution of Λ using $N_{\min} = n_p = 3$ microstructures. However, not all sets of 3 microstructures resulted in the correct solution.

To investigate what microstructural characteristics were required to solve the localization problem, we evaluated Eq. 9 for all $\binom{51}{3} = 20,825$ possible sets of $N = 3$ distinct microstructures out of the 51 that we simulated. Because of the special class of microstructures considered here (honeycomb network with ODFs specified by Eq. 1, and spatially uncorrelated grain orientations), the structure of the grain boundary network can be fully specified by the fraction of high-angle grain boundaries, p_2. Thus, an $N = 3$ microstructure set can be described by the ordered triplet $\left(p_2^{(1)}, p_2^{(2)}, p_2^{(3)}\right)$, where $p_2^{(1)} \leq p_2^{(2)} \leq p_2^{(3)}$ are the fractions of high-angle grain boundaries in the first, second, and third microstructures in the set, respectively. Figure 6 reveals that microstructure sets that returned the true solution (to within the precision of Λ) and those that did not were separated into, more or less, well-defined regions. The planar boundaries separating satisfactory microstructure sets (green polyhedral region) from unsatisfactory ones (red points) define the microstructural characteristics that permit solution of the localization problem:

$$p_2^{(1)} < p_{c,2} \tag{C.1}$$

$$p_2^{(3)} > p_{c,2} \tag{C.2}$$

These two conditions simply mean that both sides of the percolation threshold must be sampled. While necessary, conditions C.1 and C.2 are apparently insufficient to guarantee the correct solution as there are a small number of microstructure sets falling in this region that still do not produce the correct results. These, however, invariably fall near other facets of this region and can be eliminated by additionally enforcing the following conditions:

$$p_2^{(2)} - p_2^{(1)} \geq 0.0756 \tag{C.3}$$

$$p_2^{(1)} \geq 0.0092 \tag{C.4}$$

$$p_2^{(2)} \leq p_{c,2} \quad \text{or} \quad p_2^{(2)} \geq p_{c,2} + 0.0202 \tag{C.5}$$

$$p_2^{(3)} - p_{c,2} \geq 0.0202 \tag{C.6}$$

The necessity of C.3 confirms that solution of the localization problem is complicated when the first and second microstructures in the set are too similar and quantifies how different is "different enough" to avoid microstructural redundancy. Condition C.4 is required only to eliminate the single anomalous point at $(0, 0.3487, 0.9168)$, and could equally have been expressed as an upper bound on $p_2^{(3)}$. In either case, the surprising implication is that $p_2^{(1)}$ and/or $p_2^{(3)}$ should not be too *far* from $p_{c,2}$. C.5 and C.6 indicate that the second and third microstructures in the set, respectively, should posses high-angle boundary fractions that are sufficiently far from the percolation threshold.
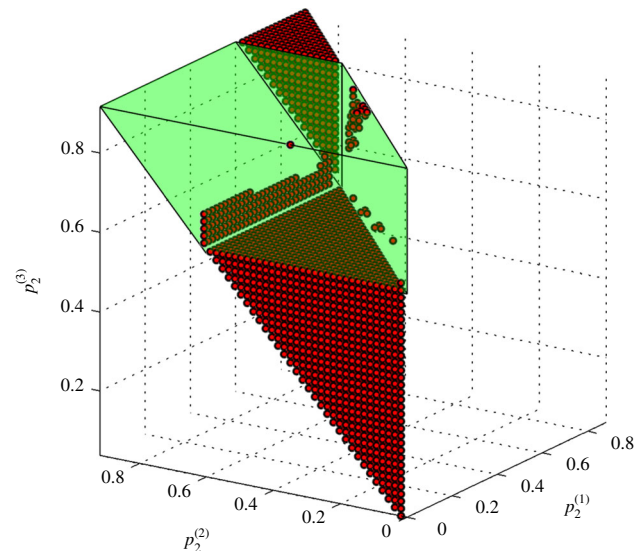

Fig. 6 All $\binom{51}{3} = 20,825$ possible sets of $N = 3$ distinct microstructures as represented by their respective fractions of high-angle grain boundaries. The coordinates of a point, $\left(p_2^{(1)}, p_2^{(2)}, p_2^{(3)}\right)$, indicate the fraction of high-angle boundaries in each of the three microstructures in the set, where $p_2^{(1)} \leq p_2^{(2)} \leq p_2^{(3)}$. The *red points* represent microstructure sets that did not result in successful recovery of the true constitutive parameters. For the sake of visual clarity, the points representing microstructure sets that did result in successful recovery of the true constitutive parameters are not shown, instead they are indicated by the green semi-transparent region (Color figure online)

Extrapolating these specific results to the general localization problem, we postulate that satisfactory microstructure sets should (1) be sufficiently diverse so as to avoid microstructural redundancy; (2) sample all regimes of the effective property of interest; and (3) avoid critical points (e.g., percolation thresholds).

Having performed many simulations spanning the domain of p_2, we had the luxury of knowing the location of the percolation threshold, $p_{c,2}$. Consequently, it would be possible for us to deliberately choose a set of $N = 3$ microstructures satisfying the conditions C.1 to C.6. In general, one may not know the salient features of a candidate structure–property model. In such cases, one might attempt to uniformly sample the structure space. For sets of randomly selected microstructures, the accuracy and precision of the solution to the localization problem increases with N. Using $N = 3$ randomly chosen microstructures (repeated 100 times), we succeeded in recovering the true parameter values to within the precision of Λ in 67 % of the trials. For $N = 5, 10, 20, 50$, the success rates were 87, 98, 100, and 100 %, respectively. Figure 7 shows 95 % confidence intervals for each of the parameters, as a function of N. The convergence of the confidence interval for $\log(D_2)$ was slower than for the other two parameters, and, expressed in terms of %error, it scaled according to
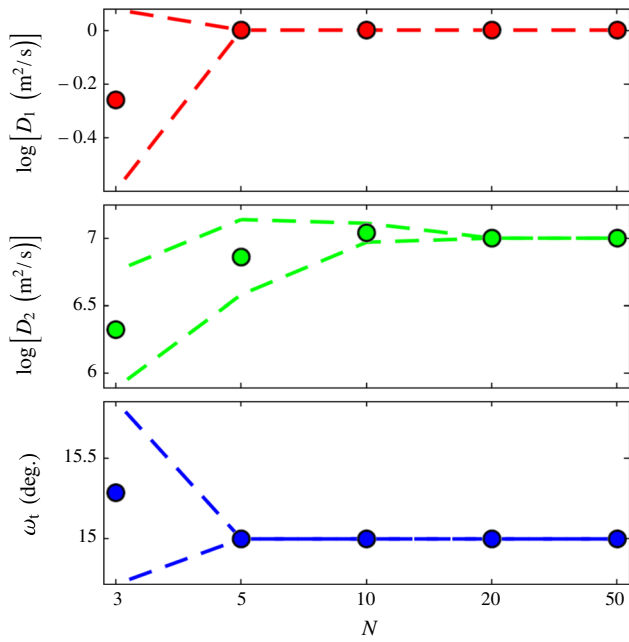
Fig. 7 Ninety-five percent confidence intervals for each of the parameters as obtained by solving the localization problem with N microstructures chosen uniformly at random from among those considered here. The process was repeated 100 times for each N

$$\%\mathrm{ERR}_{\log(D_2)} = 0.13 \exp\left(-0.2449N\right) \tag{11}$$

with a coefficient of determination of 0.9983. This scaling relationship serves as an upper bound[3] on the error in the solution of the localization problem and is useful as a means of estimating the marginal value of performing an additional experiment. For example, assume one has characterized the microstructures of $N = 7$ randomly chosen samples and measured their effective diffusivity. How much more accurate would the estimates of D_1, D_2, and ω_t be if $N = 8$ microstructures were used instead? Using the scaling relationship we conclude that, with 95 % confidence, all of the parameter estimates will be correct to within 2.34 %. By adding an additional microstructure, the maximum error in the inferred parameter values would be reduced to 1.83 %. Alternatively, if one simply wants to know the minimum number of microstructures needed to ensure that the error is less than, e.g., 5 %, use of the scaling relationship would reveal that $N = 4$ microstructures are required.

---

[3] The percent error for $\log(D_2)$ is strictly greater than or equal to that of ω_t. However, since $\log(D_1) = 0$ the concept of percent error is not well defined for this parameter. Alternatively, considering the percent error in D_1 instead of its logarithm would be inconsistent with the rest of our analysis. While the absolute error of $\log(D_1)$ is very large for $N = 3$, it is zero (or at least smaller than the resolution of Λ) for all other values of N that were tested, and consequently its %error can be reasonably considered to be zero as well. Therefore, using the percent error of $\log(D_2)$ as a bound is strictly only valid for $N \geq 5$.

For the sake of comparison, a scaling law for bicrystal experiments can be derived. Consider a set of N bicrystals with respective misorientations, $\{\omega_1, \omega_2, \ldots, \omega_N\}$, which are sampled from $U(0, 180°)$. One could perform diffusion experiments on each of the N bicrystals in an attempt to infer the parameters, $\boldsymbol{P} = [D_1, D_2, \omega_t]^{\mathrm{T}}$, of the constitutive equation (Eq. 2). In the case of these bicrystal experiments, the 95 % confidence interval for ω_t will converge more slowly than for the other two parameters and thus the %error on ω_t will be the upper bound for the bicrystal experiments. As demonstrated in the Appendix, the %error in the parameter estimates resulting from these bicrystal measurements scales according to

$$\%\mathrm{ERR}_{\omega_t} \approx 0.0227N^{-1} \tag{12}$$

Let us set a target value for a tolerable %error in our recovered parameter values, e.g., $\%\mathrm{ERR} \leq 5\%$. Solving Eqs. 11 and 12 for N, we find that the number of samples, N_{B}, required to achieve a given level of error with bicrystal experiments scales according to

$$N_{\mathrm{B}} \propto \frac{1}{\%\mathrm{ERR}} \tag{13}$$

In comparison, the required number of experiments using localization, N_{L}, scales as

$$N_{\mathrm{L}} \propto \ln\left(\frac{1}{\%\mathrm{ERR}}\right) \tag{14}$$

Figure 8 shows a graphical comparison of N_{B} and N_{L} as a function of %ERR, which confirms that localization dramatically reduces the experimental effort required to infer $\boldsymbol{P}$. For our chosen level of accuracy, $\%\mathrm{ERR} \leq 5\%$, we would need to perform at least 882 bicrystal experiments, on average, to infer the values of the constitutive parameters. In contrast, localization would necessitate an average of only four experiments for the same level of accuracy.

As just mentioned, one of the great advantages of the localization approach to deducing the properties of microstructural constituents and structure–property correlations is efficiency. We expect this experimental economy to be a general feature of the localization method, extending beyond the model system considered here. To obtain good coverage of a d-dimensional space ($d = 5$ for grain boundaries) and make meaningful inferences about structure–property correlations would require $\mathcal{O}(10^d)$ experiments (starting from a point of complete ignorance). In contrast, given a pre-specified constitutive relation with n_{p} undetermined parameters, the localization methods described here allow inference of structure–property relations with as few as $\mathcal{O}(n_{\mathrm{p}})$ experiments and there is evidence that even for more complex constitutive relations than what we have considered
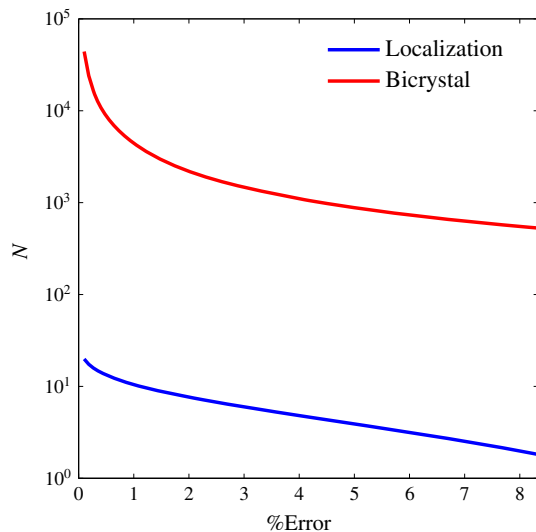
Fig. 8 The number of experiments, N, required for one to recover the values of all of the constitutive parameters in Eq. 2 to within a given level of uncertainty (%error). The performance of the localization methods introduced in this paper is compared with that of an exhaustive bicrystal approach

here, n_p may be extremely small. For example, [63] recently developed a function for grain boundary energy in FCC metals that requires only two material-specific parameters [63]. Thus, the key to experimental determination of grain boundary structure–property relations may be the development of physics-based constitutive models with clearly stated parameters. The present results suggest that systematic experimental calibration of such models may be possible and would require far less experimental effort than an exhaustive bicrystal approach. Furthermore, the use of the localization approach presented here, in conjunction with model selection techniques, could allow not only for the calibration of model parameters, but also the deduction of the form of an appropriate model and the rigorous quantification of the uncertainty in both model form and parameter values.

In this paper, the localization approach has been demonstrated in the specific context of a grain boundary structure–property model. However, the localization approach is not limited to a particular material, property, or microstructural feature. Rather, the localization methodology is completely general and may be applied to any material, for the inference of any property, as long as a suitable homogenization relation (H) and an appropriate *ansatz* for the relevant constitutive equation (P) exist.

Conclusions

In this paper, we defined the problem of grain boundary properties localization, which permits one to infer the parameters of a grain boundary structure–property model

from macroscopic measurements of effective materials properties. Stated another way, the localization approach allows one to infer local physics information from measurements of global structure and the effective response of the material. We applied this technique to a simple model system of grain boundary diffusivity in a two-dimensional microstructure and inferred the properties of low- and high-angle grain boundaries from the effective diffusivity of the entire grain boundary network. Below we summarize the main conclusions of this investigation:

1. Under appropriate conditions, the localization problem has a unique solution and the objective function converges monotonically toward it. In our model problem, we found that this unique solution coincided with the known true solution.

2. Solution of the localization problem requires at least $N = n_p$ non-redundant microstructures.

3. General microstructural characteristics required to recover the correct solution to the model localization problem considered here were that the microstructures should be sufficiently different, should sample all unique effective properties regimes (i.e., both sides of the percolation threshold), and should avoid regions where abrupt transitions occur in the effective properties ($p_{c,2}$). For a general localization problem, the details will be problem specific.

4. If appropriate selection criteria are unknown and selection of microstructures is performed uniformly at random, the accuracy and precision of the resulting inferences increase with N, the number of microstructures considered. At the 95 % confidence level, an upper bound to the %error in the inferred parameter values was shown to decay exponentially with N. This scaling relationship can assist in determining the marginal value of performing additional experiments or to identify the minimum number of experiments one should perform to obtain a specified accuracy in the solution.

5. Materials properties localization provides an efficient means to infer structure–property models for grain boundaries. In the present case, we found that, using brute force bicrystal experiments, the number of experiments required to infer constitutive model parameters scales inversely with the desired accuracy ($N_B \propto \frac{1}{\%\text{ERR}}$). In contrast, the number of experiments that localization requires is much smaller and scales logarithmically with the inverse of the desired accuracy ($N_L \propto \ln\left(\frac{1}{\%\text{ERR}}\right)$). For more general structure–property models, we expect that, for a specified accuracy (%ERR), the effort required for localization will scale with n_p, the number of parameters in the model, which should generally be small. In contrast,

the experimental effort required for a brute force bicrystal approach should scale exponentially with d, the number of degrees of freedom required to describe the microstructural feature of interest (for grain boundaries $d = 5$).

Appendix: Error scaling for bicrystal experiments

In attempting to infer the parameters of the constitutive equation (Eq. 2) via bicrystal experiements, the parameter D_1 will be recovered exactly if at least one bicrystal that we test has a misorientation $\omega \leq \omega_t$, assuming that there is no uncertainty in the value of D_1 that we measure. Likewise, D_2 will be recovered exactly with at least one bicrystal having $\omega > \omega_t$. To recover the final parameter, ω_t, to within some specified accuracy (%ERR), there must be at least one bicrystal with misorientation falling in the range $[\omega_t - \delta, \omega_t]$ and another bicrystal with misorientation falling in the range $[\omega_t, \omega_t + \delta]$, where $\%ERR = \delta/\omega_t$. For small δ, the error in ω_t will be larger than that of both D_1 and D_2. Specifically, this will be the case for $\delta < \omega_t$. We wish to identify the number of bicrystal experiments, N, required to recover ω_t to within δ of its true value at a 95 % confidence level.

Consider a set of N bicrystals with respective misorientations, $\{\omega_1, \omega_2, \ldots, \omega_N\}$, which are sampled from $\Omega \sim U(0, \omega_{max})$, where $\omega_{max} = 180°$ for the crystal system considered in this study . Let[4] A be the event that at least one of these bicrystals falls in the interval $[\omega_t - \delta, \omega_t]$, and let B be the event that at least one of these bicrystals falls in the interval $[\omega_t, \omega_t + \delta]$. We are interested in finding N such that

$$\mathbb{P}(A \cap B) = 0.95 . \tag{15}$$

Thus, we seek an expression for the joint probability $\mathbb{P}(A \cap B)$. This may be accomplished by considering the complement:

$$\begin{aligned} \mathbb{P}(A \cap B) &= 1 - \mathbb{P}(A^C \cup B^C) \\ &= 1 - \left[\mathbb{P}(A^C) + \mathbb{P}(B^C) - \mathbb{P}(A^C \cap B^C)\right] . \end{aligned} \tag{16}$$

The probability that none of the N samples fall within $[\omega_t - \delta, \omega_t]$ is given by

$$\mathbb{P}(A^C) = \left(1 - \frac{\delta}{\omega_{max}}\right)^N . \tag{17}$$

Likewise, for the interval $[\omega_t, \omega_t + \delta]$ we have

$$\mathbb{P}(B^C) = \left(1 - \frac{\delta}{\omega_{max}}\right)^N . \tag{18}$$

The probability that none of the samples fall in the interval $[\omega_t - \delta, \omega_t + \delta]$ is given by

$$\mathbb{P}(A^C \cap B^C) = \left(1 - \frac{2\delta}{\omega_{max}}\right)^N . \tag{19}$$

Substituting these results into Eq. 16 we find

$$\mathbb{P}(A \cap B) = 1 - 2\left(1 - \frac{\delta}{\omega_{max}}\right)^N + \left(1 - \frac{2\delta}{\omega_{max}}\right)^N . \tag{20}$$

Substituting $\delta = \omega_t(\%ERR)$, setting Eq. 20 equal to 0.95, and solving for N numerically for 100 values of $\%ERR \in \{0.001, 0.002, \ldots, 0.100\}$, we observe the $N(\%ERR)$ dependence shown in Fig. 9.

These results suggest a power-law dependence, and a fit to the data results in the following:

$$N = 44.0337(\%ERR)^{-1.0003} \tag{21}$$

with a coefficient of determination equal to $R^2 = 1.0000$ and an RMS error of 1.0407. The 95 % confidence intervals for the parameters in Eq. 21 are [44.0216, 44.0459]
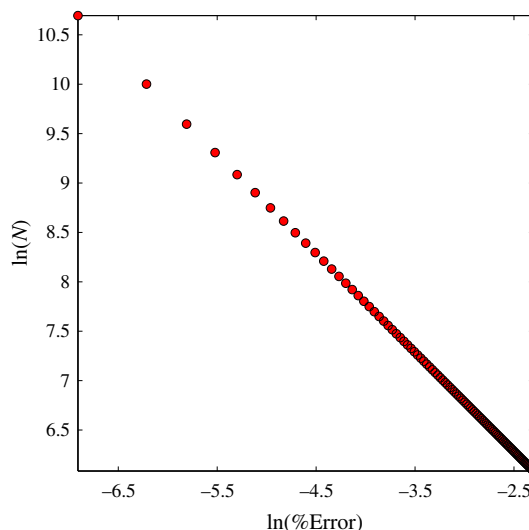
Fig. 9 Solutions of Eq. 15 for various values of $\%ERR \in \{0.001, 0.002, \ldots, 0.100\}$

---

[4] The authors wish to acknowledge David K [64], of the Math Stack Exchange community, for suggesting the derivation provided in Eqs. 15–20, which we subsequently validated both numerically and analytically.

and $[-1.0002, -1.0003]$, respectively. For comparison with the error scaling of the localization method (See Eq. 11), we can rearrange Eq. 21 to get the error scaling law for a bicrystal approach:

$$\%ERR = 0.0227N^{-0.9997} \qquad (22)$$

References

1. Seita M, Hanson JP, Graděcak S, Demkowicz MJ (2015a) The dual role of coherent twin boundaries in hydrogen embrittlement. Nat Commun 6:6164. doi:10.1038/ncomms7164

2. Lehockey EM, Limoges D, Palumbo G, et al. (1999) On improving the corrosion and growth resistance of positive Pb-acid battery grids by grain boundary engineering. J Power Sour 78(1–2):79–83. doi:10.1016/S0378-7753(99)00015-4

3. Lehockey EM, Palumbo G (1997) On the creep behaviour of grain boundary engineered nickel. Mater Sci Eng A 237(2):168–172. doi:10.1016/S0921-5093(97)00126-3

4. Lehockey EM, Palumbo G, Lin P (1998) Improving the weldability and service performance of nickel-and iron-based superalloys by grain boundary engineering. Metall Mater Trans A 29(12):3069–3079. doi:10.1007/s11661-998-0214-y

5. Norton DP, Goyal A, Budai JD, et al. (1996) Epitaxial YBa$_2$Cu$_3$O$_7$ on biaxially textured Nickel (001): an approach to superconducting tapes with high critical current density. Science 274(5288):755–757. doi:10.1126/science.274.5288.755

6. Sutton AP, Balluffi RW (2007) Interfaces in crystalline materials. Monographs on the physics and chemistry of materials (Book 51), 3rd edn. New York: Oxford University Press

7. Demkowicz MJ, Wang J, Hoagland RG (2008) Interfaces between dissimilar crystalline solids, chap. 83. In: Hirth JP (ed) Dislocations in solids, vol. 14. New York: Elsevier, pp 141–205. doi:10.1016/S1572-4859(07)00003-4

8. Vitek V, Minonishi Y, Wang GJ (1985) Multiplicity of grain boundary structures: vacancies in boundaries and transformations of the boundary structure. J Phys Colloq 46(C4):C4-171–C4-183. doi:10.1051/jphyscol:1985420

9. Vitek V, Sutton A, Wang GJ, Schwartz D (1983) On the multiplicity of structures and grain boundaries. Scripta Metall 17:183–189. doi:10.1016/0036-9748(83)90096-0

10. Chin GY (1959) Studies of growth and fatigue in bicrystals of Aluminum. Cambridge: Bachelor of Science, Massachusetts Institute of Technology

11. Schwarz S, Houge E, Giannuzzi L, King A (2001) Bicrystal growth and characterization of copper twist grain boundaries. J Cryst Growth 222(1–2):392–398. doi:10.1016/S0022-0248(00)00918-0

12. Fleischer RL, Davis RS (1959) Controlling grain boundary position in growth from the melt. Trans Metall Soc AIME 215:665–666

13. Schober T, Balluffi RW (1969) Dislocation sub-boundary arrays in oriented thin-film bicrystals of gold. Philos Mag 20(165):511–518. doi:10.1080/14786436908228723

14. Amiri-Hezaveh A, Balluffi RW (1993) Apparatus for producing ultraclean bicrystals by the molecular beam epitaxy growth and ultrahigh vacuum bonding of thin films. Rev Sci Instrum 64(10):2983. doi:10.1063/1.1144344

15. Heinemann S, Wirth R, Dresen G (2001) Synthesis of feldspar bicrystals by direct bonding. Phys Chem Miner 28(10):685–692. doi:10.1007/s002690000142

16. Marquardt K, Petrishcheva E, Garðes E, et al. (2011) Grain boundary and volume diffusion experiments in yttrium aluminium garnet bicrystals at 1,723 K: a miniaturized study. Contrib Mineral Petrol 162(4):739–749. doi:10.1007/s00410-011-0622-7

17. Plößl A, Kräuter G (1999) Wafer direct bonding: tailoring adhesion between brittle materials. Mater Sci Eng R 25(1–2):1–88. doi:10.1016/S0927-796X(98)00017-5

18. Holm EA, Olmsted DL, Foiles SM (2010) Comparing grain boundary energies in face-centered cubic metals: Al, Au, Cu and Ni. Scr Mater 63(9):905–908. doi:10.1016/j.scriptamat.2010.06.040

19. Olmsted DL, Foiles SM, Holm EA (2009a) Survey of computed grain boundary properties in face-centered cubic metals: I. Grain boundary energy. Acta Mater 57(13):3694–3703. doi:10.1016/j.actamat.2009.04.007

20. Olmsted DL, Holm EA, Foiles SM (2009b) Survey of computed grain boundary properties in face-centered cubic metals II: grain boundary mobility. Acta Mater 57(13):3704–3713. doi:10.1016/j.actamat.2009.04.015

21. Seita M, Volpi M, Patala S, McCue I, Diamanti MV, Schuh CA, Demkowicz MJ. A hybrid non-destructive technique to characterize grain boundary crystallography (in preparation)

22. Sorensen C, Basinger JA, Nowell MM, Fullwood DT (2014) Five-parameter grain boundary inclination recovery with ebsd and interaction volume models. Metall Mater Trans A 45:4165–4172. doi:10.1007/s11661-014-2345-7

23. Suter RM, Hennessy D, Xiao C, Lienert U (2006) Forward modelling method for microstructure reconstruction using x-ray diffraction microscopy: Single-crystal verification. Rev Sci Instrum 77(12):123905. doi:10.1063/1.2400017

24. Binci M, Fullwood DT, Kalidindi SR (2008) A new spectral framework for establishing localization relationships for elastic behavior of composites and their calibration to finite-element models. Acta Mater 56(10):2272–2282. doi:10.1016/j.actamat.2008.01.017

25. Duvvuru HK, Wu X, Kalidindi SR (2007) Calibration of elastic localization tensors to finite element models: application to cubic polycrystals. Comput Mater Sci 41(2):138–144. doi:10.1016/j.commatsci.2007.03.008

26. Fast T, Kalidindi SR (2011) Formulation and calibration of higher-order elastic localization relationships using the MKS approach. Acta Mater 59(11):4595–4605. doi:10.1016/j.actamat.2011.04.005

27. Fullwood DT, Kalidindi SR, Adams BL (2009a) Second-order microstructure sensitive design using 2-point spatial correlations, chap. 13. In: Schwartz AJ, Kumar M, Adams BL, Field DP (eds) Electron backscatter diffraction in materials science; , 2nd edn. New York: Springer, pp 177–188. doi:10.1007/978-0-387-88136-2

28. Fullwood DT, Kalidindi SR, Adams BL, Ahmadi S (2009b) A discrete Fourier transform framework for localization relations. Comput Mater Contin 9(1):25–40. doi:10.3970/cmc.2009.009.025

29. Fullwood DT, Niezgoda SR, Adams BL, Kalidindi SR (2010) Microstructure sensitive design for performance optimization. Prog Mater Sci 55(6):477–562. doi:10.1016/j.pmatsci.2009.08.002

30. Kalidindi SR, Landi G, Fullwood DT (2008) Spectral representation of higher-order localization relationships for elastic behavior of polycrystalline cubic materials. Acta Mater 56(15):3843–3853. doi:10.1016/j.actamat.2008.01.058

31. Landi G, Kalidindi SR (2010) Thermo-elastic localization relationships for multi-phase composites. Comput Mater Contin 16(3):273–294. doi:10.3970/cmc.2010.016.273

32. Li D, Szpunar J (1992) Determination of single crystals' elastic constants from the measurement of ultrasonic velocity in the

polycrystalline material. Acta Metall Mater 40(12):3277–3283. doi:10.1016/0956-7151(92)90041-C

33. Howard CJ, Kisi EH (1999) Measurement of single-crystal elastic constants by neutron diffraction from polycrystals. J Appl Crystallogr 32(4):624–633. doi:10.1107/S0021889899002393

34. Hayakawa M, Imai S, Oka M (1985) Determination of single-crystal elastic constants from a cubic polycrystalline aggregate. J Appl Crystallogr 18(6):513–518. doi:10.1107/S0021889885010809

35. Chen Y, Schuh CA (2006) Diffusion on grain boundary networks: percolation theory and effective medium approximations. Acta Mater 54(18):4709–4720. doi:10.1016/j.actamat.2006.06.011

36. Rohrer GS (2011) Grain boundary energy anisotropy: a review. J Mater Sci 46(18):5881–5895. doi:10.1007/s10853-011-5677-3

37. Hwang JCM, Balluffi RW (1979) Measurement of grain-boundary diffusion at low temperatures by the surface accumulation method. I. Method and analysis. J Appl Phys 50(3):1339. doi:10.1063/1.326168

38. Ma Q, Balluffi RW (1993) Diffusion along [001] tilt boundaries in the Au/Ag system I. Experimental results. Acta Metall Mater 41(1):133–141. doi:10.1016/0956-7151(93)90345-S

39. Johnson OK, Schuh CA (2013) The uncorrelated triple junction distribution function: towards grain boundary network design. Acta Mater 61(8):2863–2873. doi:10.1016/j.actamat.2013.01.025

40. Gertsman VY, Tangri K (1995) Computer simulation study of grain boundary and triple junction distributions in microstructures formed by multiple twinning. Acta Metall Mater 43(6):2317–2324. doi:10.1016/0956-7151(94)00422-6

41. Fortier P (1997) Triple junction and grain boundary character distributions in metallic materials. Acta Mater 45(8):3459–3467. doi:10.1016/S1359-6454(97)00004-9

42. Kumar M, King WE, Schwartz AJ (2000) Modifications to the microstructural topology in f.c.c. materials through thermomechanical processing. Acta Mater 48(9):2081–2091. doi:10.1016/S1359-6454(00)00045-8

43. Davies P, Randle V, Watkins G, Davies H (2002) Triple junction distribution profiles as assessed by electron backscatter diffraction. J Mater Sci 37(19):4203–4209. doi:10.1023/A:1020052306493

44. Schuh CA, Kumar M, King WE (2003) Analysis of grain boundary networks and their evolution during grain boundary engineering. Acta Mater 51(3):687–700. doi:10.1016/S1359-6454(02)00447-0

45. Yi Y, Kim J (2004) Characterization methods of grain boundary and triple junction distributions. Scr Mater 50(6):855–859. doi:10.1016/j.scriptamat.2003.12.010

46. Frary ME, Schuh CA (2005a) Connectivity and percolation behaviour of grain boundary networks in three dimensions. Philos Mag 85(11):1123–1143. doi:10.1080/14786430412331323564

47. Mason JK, Schuh CA (2007) Correlated grain-boundary distributions in two-dimensional networks. Acta Crystallogr Sect A 63(Pt 4):315–328. doi:10.1107/S0108767307021782

48. Wall MA, Schwartz AJ, Nguyen L (2001) A high-resolution serial sectioning specimen preparation technique for application to electron backscatter diffraction. Ultramicroscopy 88(2):73–83. doi:10.1016/S0304-3991(01)00071-7

49. Rowenhorst D, Gupta A, Feng C, Spanos G (2006) 3D Crystallographic and morphological analysis of coarse martensite: combining EBSD and serial sectioning. Scr Mater 55(1):11–16. doi:10.1016/j.scriptamat.2005.12.061

50. Mulders J, Day A (2005) Three-dimensional texture analysis. Mater Sci Forum 495–497:237–244. doi:10.4028/www.scientific.net/MSF.495-497.237

51. Poulsen HF, Nielsen SF, Lauridsen EM, et al. (2001) Three-dimensional maps of grain boundaries and the stress state of individual grains in polycrystals and powders. J Appl Crystallogr 34(6):751–756. doi:10.1107/S0021889801014273

52. Ludwig W, Reischig P, King A, et al. (2009) Three-dimensional grain mapping by x-ray diffraction contrast tomography and the use of Friedel pairs in diffraction data analysis. Rev Sci Instrum 80(3):033905. doi:10.1063/1.3100200

53. King A, Herbig M, Ludwig W, et al. (2010) Non-destructive analysis of micro texture and grain boundary character from X-ray diffraction contrast tomography. Nucl Instrum Methods Phys Res Sect B 268(3–4):291–296. doi:10.1016/j.nimb.2009.07.020

54. Li SF, Suter RM (2013) Adaptive reconstruction method for three-dimensional orientation imaging. J Appl Crystallogr 46(2):512–524. doi:10.1107/S0021889813005268

55. Kirkpatrick S (1973) Percolation and conduction. Rev Mod Phys 45(4):574–588

56. Reed BW, Schuh CA (2009) Grain boundary networks, chap. 15. In: Schwartz AJ, Kumar M, Adams BL, Field DP (eds) Electron backscatter diffraction in materials science, 2nd edn. New York: Springer, pp 201–214. doi:10.1007/978-0-387-88136-2

57. Kaur I, Gust W (1989) Handbook of grain and interphase boundary diffusion data, vol. 1, 1st edn. Stuttgart: Ziegler Press

58. McLachlan DS (1987) An equation for the conductivity of binary mixtures with anisotropic grain structures. J Phys C 20(7):865–877. doi:10.1088/0022-3719/20/7/004

59. McLachlan DS (2003) The correct modelling of the second order terms of the complex AC conductivity results for continuum percolation media, using a single phenomenological equation. Phys B 338(1–4):256–260. doi:10.1016/j.physb.2003.08.002

60. Stauffer D, Aharony A (1994) Introduction to percolation theory, 2nd edn. Philadelphia: Taylor & Francis

61. Frary ME, Schuh CA (2005b) Grain boundary networks: scaling laws, preferred cluster structure, and their implications for grain boundary engineering. Acta Mater 53(16):4323–4335. doi:10.1016/j.actamat.2005.05.030

62. Frary ME, Schuh CA (2007) Correlation-space description of the percolation transition in composite microstructures. Phys Rev E 76(4):42–45. doi:10.1103/PhysRevE.76.041108

63. Bulatov VV, Reed BW, Kumar M (2013) Grain boundary energy function for fcc metals. Acta Mater 65:161–175. doi:10.1016/j.actamat.2013.10.057

64. K D (2015) Number of samples required for an event to occur with a given confidence level. Math Stack Exch. http://math.stackexchange.com/q/1209320